# Numerical study of wheel-rail impact contact solutions at an insulated rail joint

Yang, Zhen; Boogaard, Anthonie; Wei, Zilong; Liu, Jinzhao; Dollevoet, Rolf; Li, Zili

**DOI**
10.1016/j.ijmecsci.2018.02.025

**Publication date**
2018

**Document Version**
Final published version

**Published in**
International Journal of Mechanical Sciences

**Citation (APA)**
Yang, Z., Boogaard, A., Wei, Z., Liu, J., Dollevoet, R., & Li, Z. (2018). Numerical study of wheel-rail impact contact solutions at an insulated rail joint. *International Journal of Mechanical Sciences*, *138–139*, 310-322. https://doi.org/10.1016/j.ijmecsci.2018.02.025

International Journal of Mechanical Sciences 138–139 (2018) 310–322

Contents lists available at ScienceDirect

International Journal of Mechanical Sciences

journal homepage: www.elsevier.com/locate/ijmecsci

# Numerical study of wheel-rail impact contact solutions at an insulated rail joint

Zhen Yang[a,b], Anthonie Boogaard[a], Zilong Wei[a], Jinzhao Liu[c], Rolf Dollevoet[a], Zili Li[a,*]

[a] Delft University of Technology, Section of Railway Engineering, Stevinweg 1, Delft, 2628 CN, the Netherlands
[b] MOE Key Laboratory of High-Speed Railway Engineering, Southwest Jiaotong University, Chengdu, Sichuan, China
[c] Infrastructure Inspection Research Institute, China Academy of Railway Sciences, Beijing, China

ARTICLE INFO

*Keywords:*
Insulated rail joint (IRJ)
Explicit FEM
Wheel-rail impact contact
Transient solution
Wave

ABSTRACT

This paper presents an analysis of the transient contact solutions of wheel-rail frictional rolling impacts calculated by an explicit finite element model of the wheel-insulated rail joint (IRJ) dynamic interaction. The ability of the model to simulate the dynamic behavior of an IRJ has been validated against a comprehensive field measurement in a recent paper (Yang et al., 2018). In addition to the measured railhead geometry and bi-linear elastoplastic material model used in Yang et al. (2018), this study adopts a nominal railhead geometry and an elastic material model for the simulations to provide an overall understanding of the transient contact behavior of wheel-IRJ impacts. Each simulation calculates the evolution of the contact patch area, stress magnitude and direction, micro-slip distribution, and railhead nodal vibration velocity in the vicinity of the joint during the wheel-IRJ impacts. The simulations apply small computational and output time steps to capture the high-frequency dynamic effects at the wheel-IRJ impact contact. Regular wave patterns that indicate wave generation, propagation and reflection are produced by the simulations; this has rarely been reported in previous research. The simulated waves reflect continuum vibrations excited by wheel-rail frictional rolling and indicate that the simulated impact contact solutions are reliable.

## 1. Introduction

A recent paper [1] established an explicit finite element (FE) wheel-insulated rail joint (IRJ) dynamic interaction model to calculate the high-frequency impact vibration and noise generated by a typical IRJ in the Dutch railway network. The dynamic behavior of the wheel-IRJ system reproduced by the explicit FE model was validated against a comprehensive hammer test and a pass-by measurement. This paper applies the validated dynamic interaction model to investigate the contact characteristics of wheel-IRJ impacts.

Because the finite element method (FEM) is able to handle non-linear material properties and arbitrary discontinuous contact geometries, it has been widely applied to study wheel-rail contact and the subsequent track deterioration at IRJs. A 3D FE analysis performed by Chen and Kaung [2] indicated that the traditional Hertzian contact theory [3] is inadequate for predicting wheel-rail contact pressure distributions around IRJs. Chen and Chen [4] established a 2D FE model to study the effects of an IRJ on the wheel-rail contact stress distributions under partial slip conditions and suggested that Carter' theory [5] is no longer effective for predicting the tangential stress distributions of wheel-rail contact at IRJs. Wen et al. [6] applied an explicit FEM for the contact-impact stress analysis at rail joint regions, and this model can account for dynamic effects. The explicit FE model was then developed by Cai et al. [7] to calculate the dynamic impact force, stresses and strains imposed when a wheel passes an IRJ with a height difference. Sandstrom and Ekberg [8] employed a 3D elastoplastic FEM model to predict the plastic deformation and fatigue resulting from wheel-IRJ impacts by capturing the accumulation of plastic strain. Mandal and Dhanasekar [9] proposed a sub-modeling FE strategy to examine the ratcheting failure of IRJs, and the same strategy was adopted by Mandal [10] to study the influences of end-post materials on railhead deterioration at IRJs. Zong et al. [11] applied an implicit-explicit FE model to simulate rail/wheel dynamic contact impact and railhead damage in the vicinity of IRJ. Zong and Dhanasekar [12,13] employed genetic algorithms coupled with FEMs to reduce impact stress through shape optimization of railhead at joints. On the basis of the coupled genetic algorithm and a parametric FEM, Zong and Dhanasekar [14] also developed a new design of IRJ; the design relied on embedding gapped rails within one sleeper to provide sufficient rigidity to the rail ends, and may eliminate a number of components of IRJ and their associated modes of failure.

---

[*] Corresponding author.
*E-mail address:* Z.Li@tudelft.nl (Z. Li).

https://doi.org/10.1016/j.ijmecsci.2018.02.025
Received 14 November 2017; Received in revised form 26 January 2018; Accepted 10 February 2018
Available online 12 February 2018
0020-7403/© 2018 Elsevier Ltd. All rights reserved.

Although many researchers believe that dynamic effects play certain roles during wheel-rail impacts [4,6–8, 10,15,16], quasi-static wheel-rail contact is still generally assumed in the FE models [2,4,8–10]. Transient solutions that can reflect dynamic effects in the wheel-rail impact contact have rarely been studied, which may be because well-accepted methods [3,5,17–19] capable of resolving common wheel-rail contact problems are generally based on the quasi-static contact assumption, and the dynamic effects during contact are therefore not necessarily considered in many situations. Furthermore, no direct experimental methods for accurately measuring the transient contact solutions are available [20]; therefore, although the transient contact solutions have already been calculated, accurate experimental validations cannot be performed.

Reasonable transient wheel-rail contact solutions have been obtained by explicit FEMs and used to study the compression-shift-rolling contact [21], non-steady-state transition from single-point to two-point contact [22], and dynamic cracking behavior [20]. This study also calculates the transient solutions of wheel-IRJ impact contact by employing an explicit FEM. Because the explicit FEM fully couples the calculation of wheel/rail dynamic responses with the calculation of wheel-rail contact, the validity of the transient impact contact solutions simulated in this paper may be confirmed by separately validating the quasi-steady contact solutions and wheel/rail dynamic responses. Quasi-static frictional rolling contact solutions calculated by the explicit FEM including contact area, pressure, surface shear stress and micro-slip have been shown to be accurate via comparisons with Hertzian and CONTACT solutions [23,24], whereas the simulated structural dynamic responses to wheel-IRJ impact have been validated by a comprehensive field measurement in [1]. In addition, by presenting the rail surface vibrating velocities calculated at consecutive time steps, regular wave patterns were observed in this study, which provide more evidence for the reliability of the results.

Compared with the implicit FEM, the explicit integration scheme is more robust in handling difficult contact problems because it avoids the convergence difficulties caused by demanding contact conditions [25] and the regularization of the friction law required to treat the no-slip condition in the adhesion area [26]. Moreover, the computational efficiency is significantly improved when considering high-frequency dynamics. This study calculated the evolution of the contact patch area, stress magnitude and direction, micro-slip distributions and railhead nodal vibration velocities in the vicinity of the joint using small time steps to capture the high-frequency dynamic effects during the wheel-IRJ impact.

## 2. Wheel-IRJ impact contact model

A 3D explicit FE wheel-IRJ dynamic interaction model was established in this study to simulate the wheel-rail impact at a typical IRJ in the Dutch railway network. Detailed descriptions of the model can be found in [1]. Information on the target IRJ and FE model relevant to calculating the transient solutions of wheel-IRJ impact contact are given here. Fig. 1 shows the in situ condition of the target IRJ selected for the study, and it is located in the Amsterdam-Utrecht trunk line of the Dutch railway network. UIC54 rails with an inclination of 1/40 are supported by NS90 sleepers every 0.6 m except in the proximity of the IRJ, where a pair of adjacent timber sleepers with a distance of 0.24 m is employed to reduce the deflection of the joint and absorb the vibrations caused by wheel-IRJ impacts. A close-up view of the target IRJ in Fig. 1(b) shows that the IRJ does not present visible deterioration but shows an asymmetric running band with respect to the joint; in addition, a broader running band and a brighter spot can be seen on the railhead just after the joint along the traffic direction, which is where the wheel-IRJ impacts are expected to occur.

Fig. 2 shows the 3D FE wheel-IRJ dynamic interaction model established in [1]. This model is composed of a 10-m-long half-track with an IRJ in the middle and a half-wheelset with the sprung mass of the car body and bogie. The wheel, rails, and sleepers were modeled using hexahedral elements. The explicit FE wheel-rail interaction analysis adopted the one-point quadrature scheme for the sake of computational efficiency, which, however, leaded to ‘hourglass’ modes for hexahedral elements. An orthogonal Flanagan-Belytschko hourglass control scheme [27] was thus used to avoid the undesirable hourglass modes from growing large and destroying solutions. The wheel geometry corresponds to that of a passenger car wheel of the Dutch railway with the standard profile of S1002. Because the value of elastic modulus of the end-post (insulation layer between two rail ends) is much lower than those of the rails and the presence of air gap (shown in Fig. 1(b)) may result in free rail-end [28], the end-post layer was omitted in the model and simplified as a gap. The IRJ with a 6-mm gap was modeled in detail with the nominal geometry and fine meshes. Non-uniform meshing was used, and regular discretization with a mesh size of 1 mm was allocated at the initial wheel-rail contact area and within the 0.2-m-long solution zone around the joint (Fig. 2(b)). Free boundaries were used on the rail ends at the joint, whereas non-reflecting boundaries were defined at the far ends of the rails.

Because the explicit FEM is less efficient than the implicit FEM for static equilibrium analyses, an implicit-explicit sequential approach was applied in this study to minimize both the solution time and the dynamic effects induced by the initialization of wheel-rail interaction analysis. The implicit-explicit sequential approach involves performing an implicit static equilibrium analysis followed by an explicit transient dynamics analysis, as used in [11]. The simulation first employed an implicit FE dynamic relaxation to allow the wheel-track system to reach an equilibrium state under gravity, which provided the initial nodal displacements to the explicit wheel-rail transient rolling simulation. The initial position of the wheel model was 1.32 m away from the IRJ (two standard sleeper spans and half a timber sleeper span as shown in Fig. 2(a)). The rotation and forward translation movements of the wheel were applied as the initial nodal velocities of the transient explicit analysis.

In the explicit transient dynamics analysis, we calculated the wheel-rail frictional rolling contact with a penalty contact algorithm [29], which is directly implemented in the explicit FEM and is called as a subroutine at each time step prior to the updates of the structural dynamic responses. Considering that the explicit integration scheme is conditionally stable: the integration is only stable if the time step size used is smaller than the critical time step size, and that the critical time step may vary in the nonlinear wheel-rail dynamic interaction analysis because of changes in the material parameters and/or geometry, a scale factor of critical time step 0.9 was adopted to control the computational time step and guarantee the stability of the explicit integration. The stability of the penalty contact algorithm can be controlled by scaling down the penalty contact stiffness; however, this was unnecessary in this study.

Coulomb’s law of friction was implemented for the wheel-rail contact pair with a friction coefficient of 0.35 (a typical intermediate value of the rail top friction [30]). The wheel was subsequently driven by a torque applied on the axle to roll along the rail from the initial position towards the joint, thus generating a longitudinal creep force between the wheel and rail that satisfies the requirement that the traction coefficient is below the friction coefficient.

Fig. 3(a) and (b) show the meshes of the rail top surface in proximity to the joint before and after applying the measured geometry, respectively. The in situ geometry of the target IRJ was measured using a HandySCAN 3D laser scanner. Because the railhead surface geometries vary with the operational time and each IRJ, the measured geometry may impose randomness on the simulated impact contact solutions. Moreover, the material properties of contact bodies also influence the wheel-rail contact solutions [24,31]. Therefore, in addition to the simulation conducted by the measured-geometry model in [1], two additional simulations were performed in this paper using nominal-geometry models, with one simulating elastic materials and the other simulating

(a) General condition

(b) Close-up of the end-post

**Fig. 1.** In situ condition of the target IRJ.

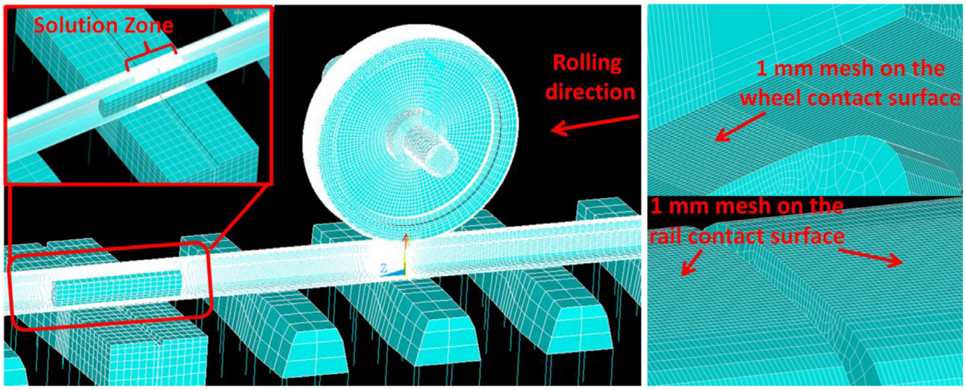

(a) Wheel-IRJ interaction model

(b) Meshes on contact surfaces

**Fig. 2.** FE wheel-IRJ interaction model.

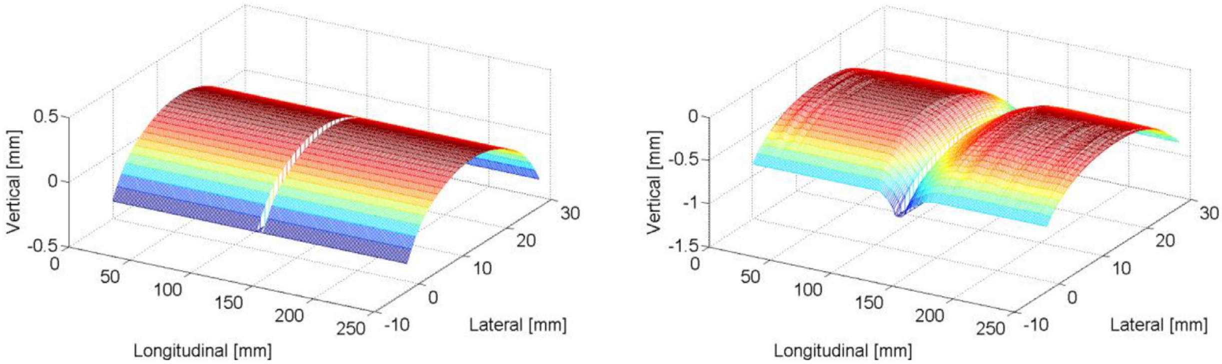

(a) Nominal geometry at the IRJ

(b) Measured geometry at the IRJ

**Fig. 3.** Applying the realistic geometry to the IRJ (the size of the irregularity is exaggerated) [1].

elastoplastic materials, to gain an overall understanding of the transient contact behavior of wheel-IRJ impacts. The setup parameters of the three simulations conducted in this study are listed in Table 1, and simulation 3 was performed in [1]. Table 2 lists the values of the material parameters used in the simulations. The elastoplastic material model applied in the paper corresponds to the R260Mn rail steel that is widely used in the Dutch railway.

## 3. Impact contact solutions

To provide a broad overview of the wheel-rail impact contact at an IRJ, the time histories of the normal contact forces calculated by the three simulations are presented at the beginning of this section. Subsequently, typical transient contact solutions calculated within the solution zone are analyzed, including the contact patch area, stress magnitude and direction, micro-slip and adhesion-slip distributions. The influence of the rail surface geometries and the material models are discussed

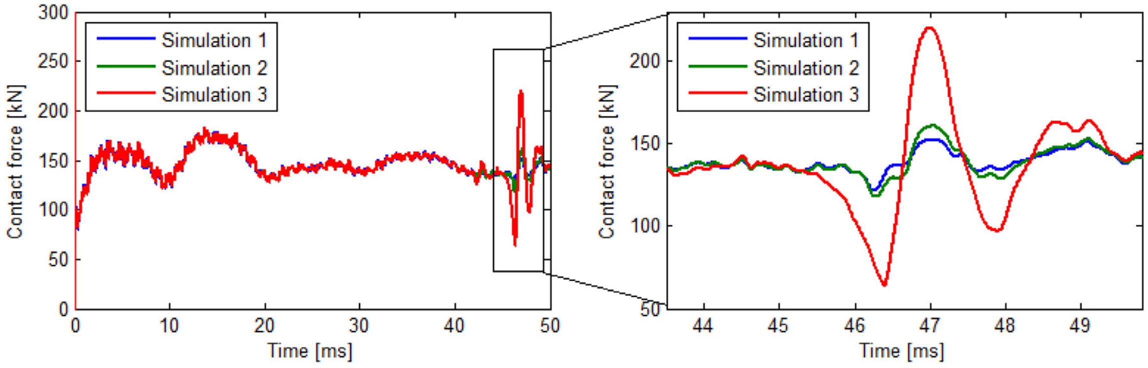

(a) Overview of the simulated contact forces (b) Impact contact forces in the solution zone

**Fig. 4.** Time history of the wheel-rail contact force.

**Table 1**
Parameters of the simulations with different set ups.

| | Material | Profile |
|---|---|---|
| Simulation 1 | Elastic | Nominal |
| Simulation 2 | Elastoplastic | Nominal |
| Simulation 3 | Elastoplastic | Measured |

**Table 2**
Values of the materials.

| Elastoplastic material parameters | | Values |
|---|---|---|
| Elastic part | Young's modulus | 210 GPa |
| | Poisson's ratio | 0.3 |
| | Density | 7800 kg/m$^3$ |
| Plastic part | Yield stress | 500 MPa |
| | Tangent modulus | 21 GPa |

by comparing the solutions obtained by the three simulations. The transient contact solutions obtained in this study also captured wave phenomena, which will be presented in Section 4.

### 3.1. Wheel-IRJ impact contact force

The time histories of the normal wheel-rail contact forces calculated by the three simulations are plotted in Fig. 4(a), which shows that obvious impact contact occurred when the wheel rolled over the joint at approximately 47 ms. The damping in the system dissipated the initial kinetic and potential energy originating from any initial inequilibrium of the system such that the oscillations were damped out to less than 10% of the static values upon arriving at the solution zone. The close-up view of the time histories around the impact plotted in Fig. 4(b) shows the simulated normal impact loads within the solution zone. The figure shows that the impact simulated with the measured geometry (simulation 3) was much larger than those simulated with the nominal geometry. In addition, a comparison of the normal loads calculated by simulations 1 and 2, which only differ in the material properties, shows that the elastoplastic material model (simulation 2) provided a slightly higher impact magnitude than the elastic model (simulation 1), probably due to that during the impacts with the same duration (see Fig. 4(b)), larger contact compression occurred in the elastoplastic solution to balance the same quasi-static wheel load [31].

As reported in [1], the wheel-IRJ dynamic interaction simulation in this study employed a small computational time step (49 ns). By applying an explicit central difference time integration and a penalty contact algorithm [29], nodal forces and motions in the solution zone were calculated for each time step. Certain nodal forces and motions were subsequently output and used to calculate the transient solutions of impact contact. A small output time step (1 μs) was used in this study to capture high-frequency dynamic effects up to 500 kHz in the transient solutions of impact contact. Transient contact solutions of 6300 output time steps, specifically from 43.5 ms to 49.8 ms (abscissa range of Fig. 4(b)), were calculated for each simulation.

An example of a transient contact solution calculated by simulation 3 that was output at instant 45.613 ms (output time step = 2113) is displayed in Fig. 5. In Fig. 5(a), from left to right, the graphs show the simulated stress distributions along the longitudinal center line of the contact patch, stress distributions within the contact patch, micro-slip distributions and rail surface nodal velocities. The contact stress distributions were determined by the calculated rail surface nodal forces; and the rail surface nodal velocities can be directly output. As for the micro-slip, or the wheel-rail relative velocity, because a rail surface contact node is actually in contact with the 'contact point' rather than a wheel surface node [32], interpolations was used to convert the output velocities of wheel nodes into the velocities of the 'contact points'.

The transient wheel-rail contact position at this instant or time step can be more easily identified in Fig. 5(b). By displaying contact solutions of a certain amount of consecutive time steps as those shown in Fig. 5(b), animations [33–35] were created, which clearly show the evolution of the contact solutions along with certain high-frequency dynamic effects. Typical transient contact solutions are selected and analyzed in the following sections to demonstrate the characteristics of the transient solutions of impact contact.

### 3.2. Contact areas and stress distributions

#### 3.2.1. Evolution of the contact areas and stress distributions

The evolution of the contact pressure together with the direction and magnitude of the surface shear stress calculated by the three simulations are plotted in the contour/vector diagrams in Fig. 6. The contact patch area can be determined via the contact pressure: an element is in contact if the contact pressure is non-zero. Thus, the evolution of the contact patch area can also be observed from Fig. 6. Eight time steps (t1-t8) with a fixed interval of 0.77 ms (770 times the output time step) between two consecutive time steps are displayed for each simulation to show the main characteristics of the impact contact area and the stress evolution. The origin of the coordinate system was at the center of the rail bottom surface at the initial position of the wheel-rail contact. Because the coordinate system included the rail inclination of the track, the longitudinal center lines of the contact patches shown in Fig. 6 are at

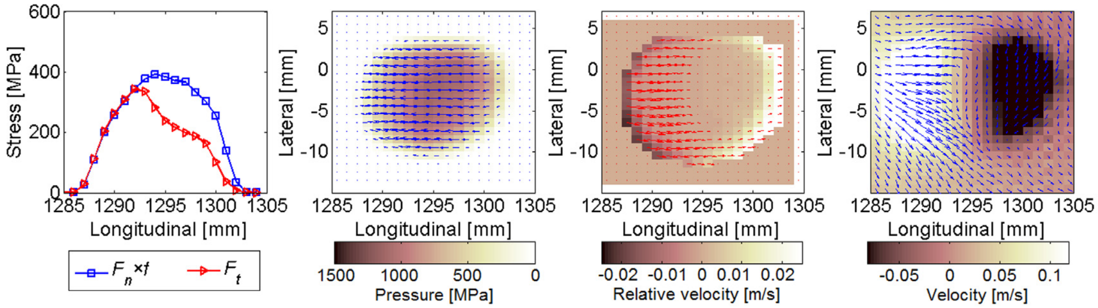

(a) transient contact solution (graphs from left to right: stress distributions along the longitudinal center line, stress distributions within the contact patch, micro-slip distribution, and rail surface nodal velocities within the whole solution zone)

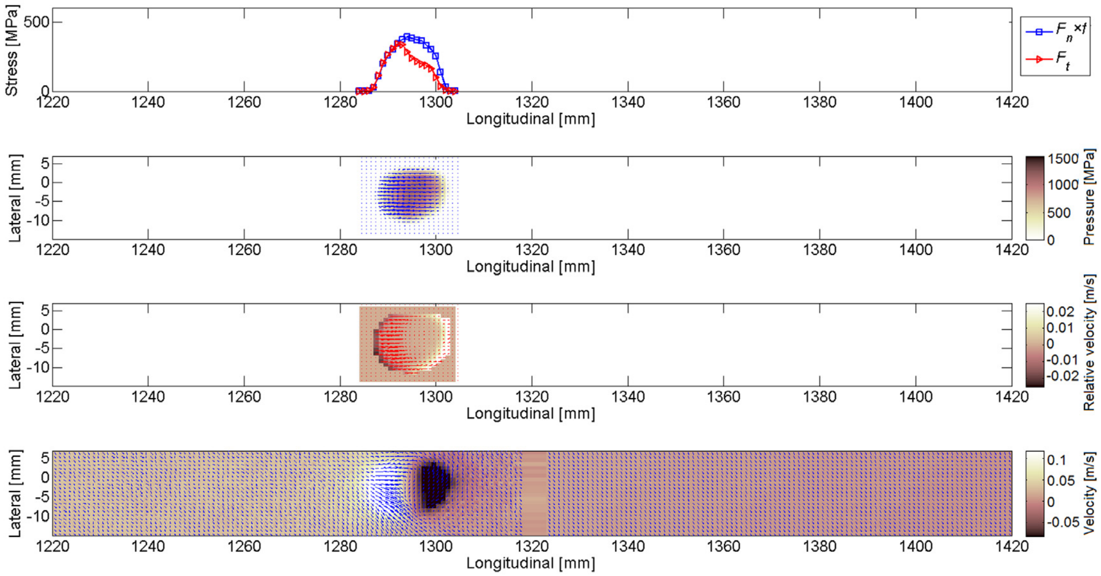

(b) transient contact solution and position within the solution zone

**Fig. 5.** Example of the transient contact solution.

approximately −3 mm in the lateral direction rather than at 0 mm. The contact pressure magnitude corresponds to the depth of color within the contact patch as indicated by the color bar. The surface shear stresses are indicated by blue arrows. The arrows point in the direction of the shear stress, and the arrow length is proportional to the magnitude.

In Fig. 6(a) and (b), other than the discontinuous contact at the joint at t4, the contact patch areas calculated by both the elastic (simulation 1) and elastoplastic models (simulation 2) correspond well with those reported in [24, 31]. The wheel-rail contact areas simulated by the elastic model have elliptical shapes, whereas those simulated by the elastoplastic model have 'egg' shapes, with the trailing parts of the contact patches enlarged because plastic deformation has occurred in the rear [31].

Although simulation 1 produced the smallest impact force (Fig. 4(b)), the amplitudes of the contact pressures calculated by simulation 1 are larger than those calculated by the other two simulations as indicated by Fig. 6 because simulation 1 had the smallest contact areas. The magnitudes of the contact pressure located approximately in the middle of the contact patch in Fig. 6(a) but in the leading section in Fig. 6(b) are also consistent with the results reported in [24,31]. The simulated contact patch areas in Fig. 6(a) and (b) basically remain steady and increase to some extent during the impact at t4 and t5. This phenomenon is more evident under the elastoplastic material condition.

Simulation 3 provided more obviously non-steady-state contact solutions as shown in Fig. 6(c). The contact areas and stress distributions vary considerably with the time step due to the geometric irregularity of the rail top surface and significant impact. The contact patches at t1 and t2 in Fig. 6(c) are similar to those at the same time steps in Fig. 6(b). Subsequently, the area of the contact patch decreases at t3 and t4 because of the geometric declivity before the joint (see Fig. 3(b)). The contact area increases remarkably during the impact contact at t5 and then shrinks at t6, when the wheel has a tendency to bounce. The rail surface geometric irregularity contributes to the irregular shapes of the contact patches, which are neither elliptical nor 'egg' shaped, as well as the irregular stress distributions in Fig. 6(c).

By plotting a trail of transient contact areas, the 'footprints' of the contact patch calculated by simulation 3 are presented in Fig. 7(a). The interval between each two consecutive contact patches is 0.3 ms (300 times the output time step). Good correspondence can be obtained by comparing the simulated 'footprints' to the in situ running band of the

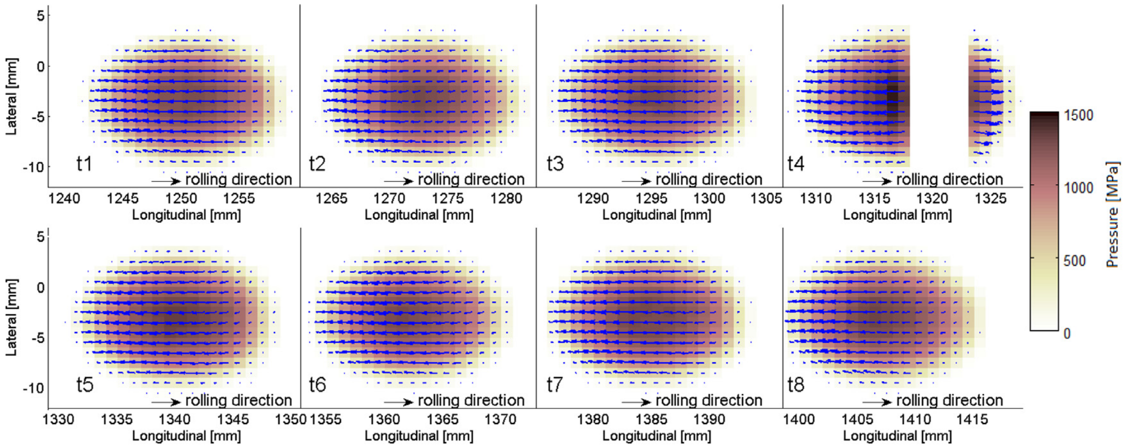

(a) Simulation 1 (elastic material & nominal geometry): elliptical contact patch

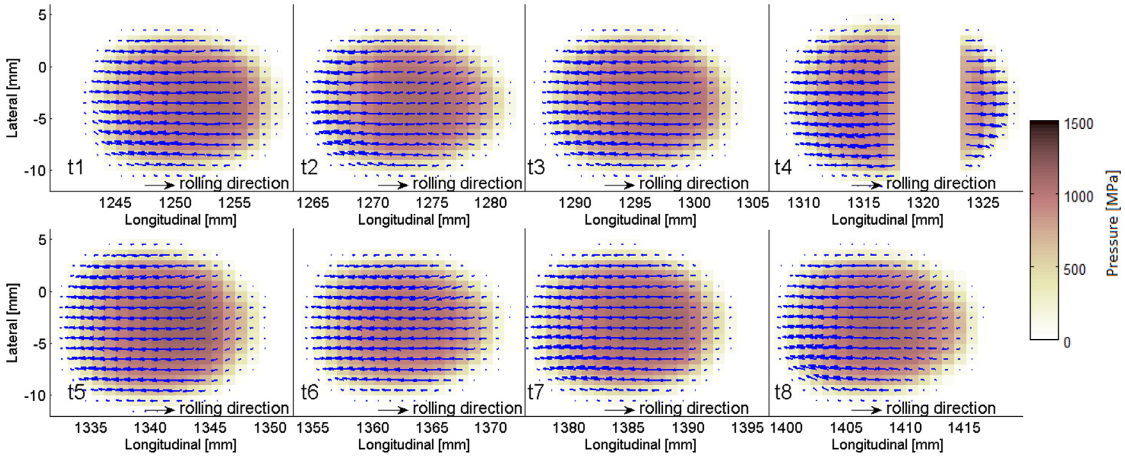

(b) Simulation 2 (elastoplastic material & nominal geometry): 'egg-shaped' contact patch

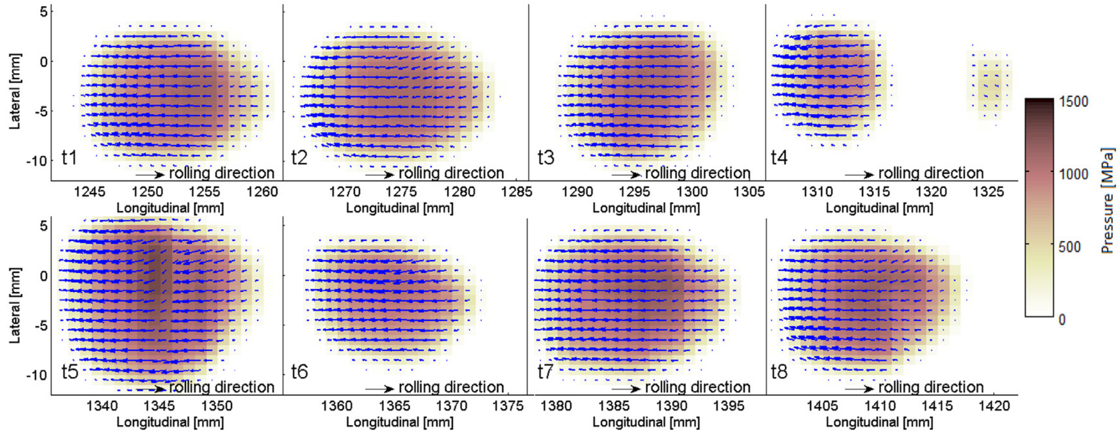

(c) Simulation 3 (elastoplastic material & measured geometry): non-steady-state contact patch

**Fig. 6.** Evolution of the impact contact area and stress distribution. (For interpretation of the references to color in this figure legend, the reader is referred to the web version of this article.)

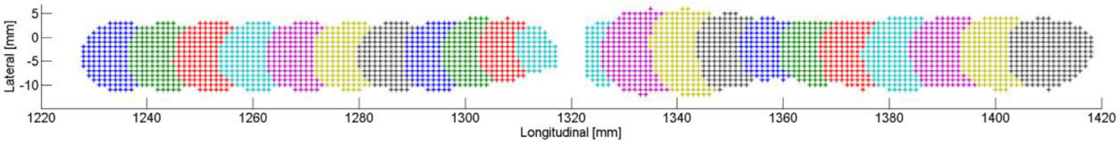

(a) ‘Footprints’ of the contact patch calculated by simulation 3 (the color differentiates an individual contact patch from the others, and the interval between each two consecutive patches is 0.3 ms)

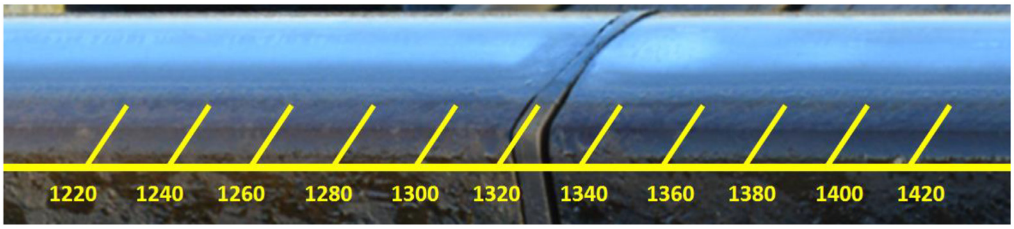

(b) In situ condition of the running band around the target IRJ

**Fig. 7.** Comparison of the simulated contact patch ‘footprints’ and the in situ running band. (For interpretation of the references to color in this figure legend, the reader is referred to the web version of this article.)

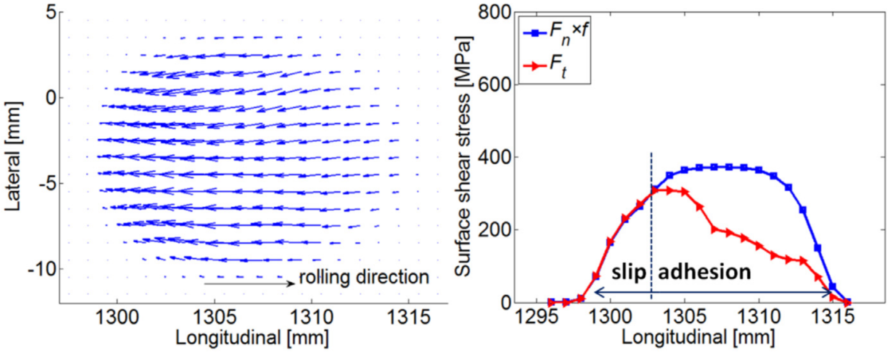

(a) Distribution within the contact patch (b) Distribution along the longitudinal axis

**Fig. 8.** Example of the surface shear stress distribution.

target IRJ shown in Fig. 7(b). The ‘footprints’ become narrow at the region just before the joint (1310–1317 mm) in Fig. 7(a), which corresponds to the cut-off of the running band (at approximately 1310 mm) in Fig. 7(b). Wheel-IRJ impacts (the first peak of the contact force in Fig. 4(b)) occur at approximately 1330–1350 mm, where the ‘footprints’ are larger in Fig. 7(a), and a broader running band and a brighter spot can be found in Fig. 7(b). The second wheel-rail impact (the second peak of the contact force in Fig. 4(b)) occurs at approximately 1380–1390 mm, where larger than usual contact patches and a brighter spot can be observed in Fig. 7(a) and (b), respectively, although they are less pronounced than those in the first impact. The good correspondence between the simulated contact patch ‘footprints’ and in situ running band implies that simulation 3 (with the measured geometry) can more accurately reproduce the transient impact contact solutions at the target IRJ, which is likely in a non-steady state.

### 3.2.2. *Positive surface shear stress*

When a wheel rolls along a rail driven by a torque at the axle, the shear stress direction on the rail surface is generally opposite to the wheel rolling direction. An example is shown in Fig. 8(a), in which the rail surface shear stress distribution was calculated via simulation 2 at instant 46 ms (output time step = 2500). By extracting the surface shear stress along the longitudinal center line of the contact patch and comparing it to the traction bound (the product of the contact pressure $F_n$ and friction coefficient $f$), the distribution of the adhesion-slip regions can be obtained, as shown in Fig. 8(b). The maximum amplitude of the surface shear stress is located at the juncture of the adhesion and slip regions. The adhesion-slip distribution within the contact patch will be analyzed in detail in the next section.

In this paper, the direction of the surface shear stress opposite to the direction of wheel rolling is defined as negative and that along the direction of wheel rolling is defined as positive. A review of the evolution of stress distribution shown in Fig. 6 indicates that as the counterforce of the traction causes the wheel to move forward, the simulated surface shear stress points in the negative direction for the majority of graphs except at the regions immediately after the joint (roughly 1323–1327 mm) at t4. To show this phenomenon more clearly, an evolution of the surface shear stress distribution within the contact patch calculated

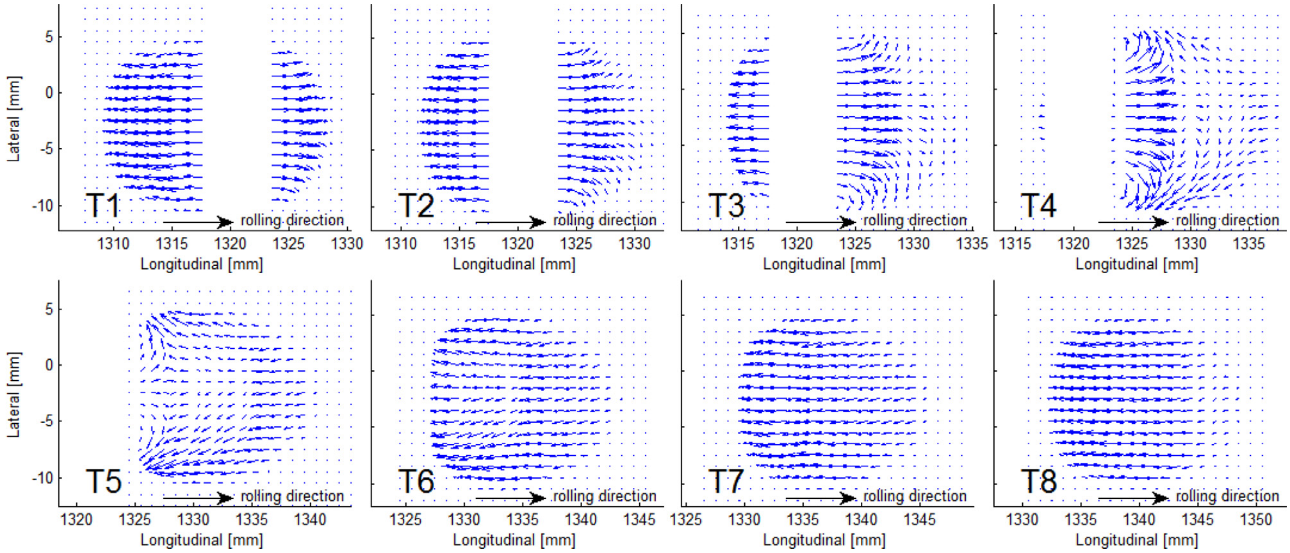

Fig. 9. Evolution of the surface shear stress calculated by simulation 2.

by simulation 2 with a smaller time step (0.1 ms, 100 times of the output time step) than that used in Fig. 6 (0.77 ms) is depicted in Fig. 9. The evolution calculated by simulations 1 and 3 (not presented here) shows the same trend.

As shown in Fig. 9, when the wheel just touches the right rail after the joint (T1-T3), the shear stress vectors on the right rail are positive, whereas those on the left rail are negative. From T4 to T6, as the contact patch moves, the amplitudes of the positive shear stresses on the right rail between 1325 mm and 1329 mm decrease to zero and then become negative. Graphs of T4 and T5 also indicate that the lateral shear stress plays an important role at these moments, especially at locations close to the top and bottom edges of the contact patch, where the surface shear stress vectors point outwards. Such stress may exacerbate material flow on the railhead and consequently widen the running band at the impact location as shown in Fig. 7(b). At the instances of T7 and T8, the contact patch has exited the positive surface shear stress region and all the stress vectors point in the negative direction. The occurrence of transient positive surface shear stress on the right rail end is shown to result from the impact contact at the IRJ with discontinuous geometry. In the region immediately after the joint, the amplitudes of the positive shear stresses caused by the wheel-IRJ impact are larger than the amplitudes of the original negative shear stresses (counterforce of the traction), thus making the resultant surface shear stresses positive.

This study modeled a wheel driven by a torque on its axle. When a braking wheel rolls on a section of track with an IRJ, the original direction of the rail surface shear stresses is expected to be positive (counterforce of the braking force). In such cases, the positive shear stresses imposed by impact will be added to the original positive shear stresses. To what extent an impact between a braking wheel and an IRJ can influence the surface shear stress distribution and the consequent wear behavior on the railhead after the joint should be studied in the future.

### 3.3. Adhesion-slip distribution and micro-slip

The division between adhesion and slip regions in the contact patch is an important feature of frictional rolling contact. The transient contact solutions that indicate the adhesion-slip distribution during the wheel-IRJ impact predicted by simulation 3 are presented in this section. The adhesion-slip distribution can be determined either by comparing the surface shear stress with the traction bound or by calculating the micro-slip within the contact patch. In this study, the simulated adhesion-slip distributions determined by these two approaches are consistent with each other, as shown in Fig. 10.

Fig. 10(a) displays comparisons of the surface shear stress and traction bound along the longitudinal center line of the contact patch at 15 instants. Instant t1 is equal to 44.4 ms, and the interval between each two consecutive instants is 0.3 ms (300 times of the output time step). Fig. 10(b) shows the evolution of the micro-slip distribution within the contact patch at the same 15 instants. The red arrows point in the direction of the micro-slip, and the arrow length is proportional to the magnitude. The micro-slip vectors (slip region) occur at the trailing part of the contact patch, and their directions largely correspond to the wheel rolling direction. The color depth within the contact patch indicates the magnitude of the normal wheel-rail relatively velocity. The color outside the contact patch corresponds to a zero relative velocity, whereas that at the leading and trailing edges of the contact patch are lighter and darker, indicating a positive and negative normal relative velocity, respectively.

The adhesion-slip distributions shown in Fig. 10 are non-steady during the wheel-IRJ impact, and the proportion of contact patch occupied by the adhesion and slip regions vary greatly with the time step from t8 onwards. The most significant variation occurs from t9 to t13. At instant t9, the adhesion region accounts for almost the entire contact patch. Next, the adhesion zone shrinks gradually and the slip region reaches its maximum occupation at instant t12, when the bounce tendency of the wheel comes to an end and the wheel is nearly at the second impact, which corresponds to the contact force trough at approximately 47.7 ms in Fig. 4(b). The good consistency between the adhesion-slip distributions calculated by the contact stresses and the micro-slips support the conclusion that the explicit FEM presented here can solve the transient impact contact problem with non-linear material properties and arbitrary discontinuous contact geometries.

## 4. Wave phenomena

Compared with the contact force and stress, the surface nodal vibration velocity is found to be more sensitive to dynamic effects excited by wheel-rail contact [22,36]. The rail surface nodal velocity calculations in this study revealed wave phenomena excited by wheel-rail frictional rolling impact contact, and the results were based on the fine mesh of the FE model, small computational and output time steps, and full coupling of the contact and dynamics in the explicit integration. The size of the fine mesh is based on the requirement that the size of the elements should be no larger than half a wavelength. The small computational time step enables the calculations to capture high-frequency dynamic effects, and the small output time step facilitates the observation of the

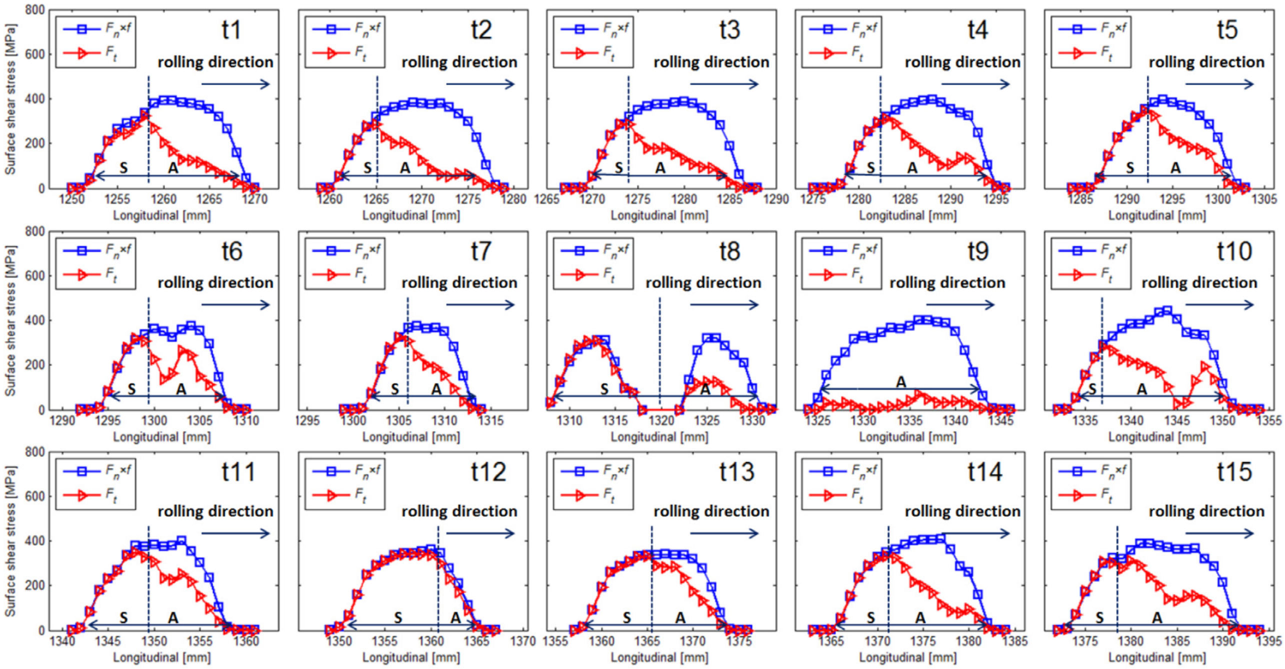

(a) By stress distribution (A: adhesion region; S: slip region)

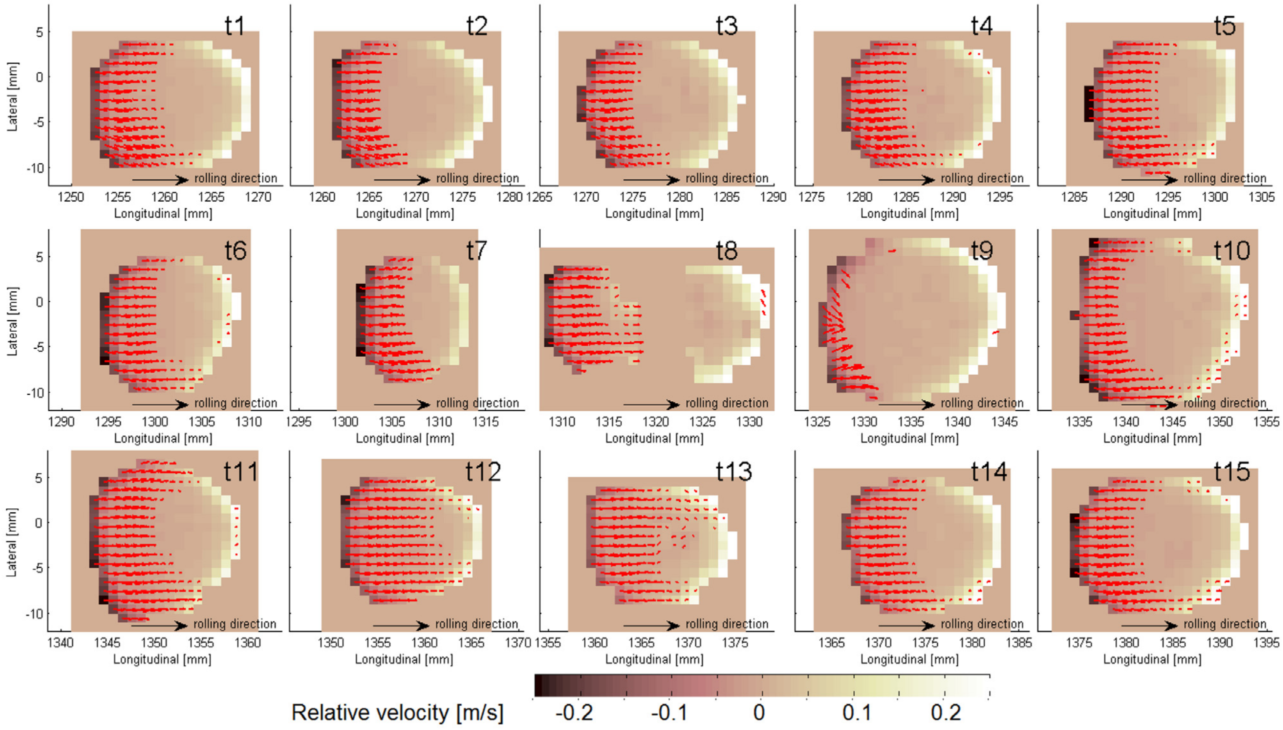

(b) By micro-slip distribution

**Fig. 10.** Evolution of the adhesion-slip distributions calculated by simulation 3. (For interpretation of the references to color in this figure legend, the reader is referred to the web version of this article.)

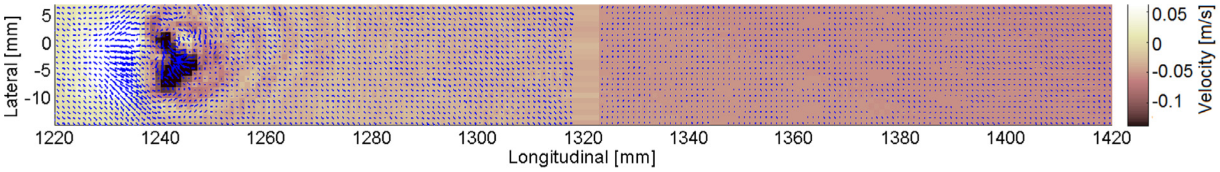

(a) Wave propagation

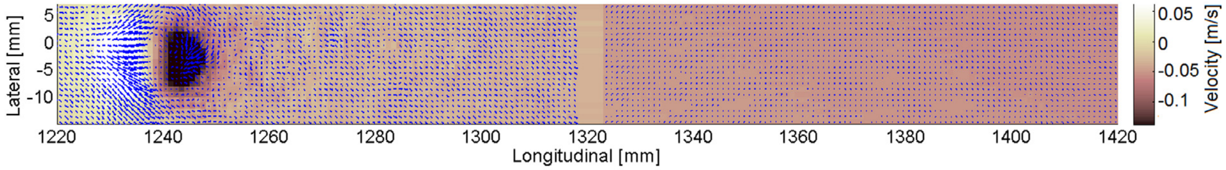

(b) Wave reflection

**Fig. 11.** Patterns of wave propagation and reflection produced by simulation 3. (For interpretation of the references to color in this figure legend, the reader is referred to the web version of this article.)

generation and propagation processes of the simulated waves. Full coupling means that the contact force and wheel-rail dynamics are updated simultaneously in every time step, thereby allowing the dynamic effects to be fully considered when calculating the contact solutions. Certain wave patterns that indicate wave generation, propagation and reflection were excited by wheel-rail contact produced in the solution zone, and they are presented and analyzed in this section. More evident wave phenomena can be observed in the animations [33–35].

### 4.1. *Waves generated by wheel-rail contact*

The wave phenomenon discussed here was first observed before the wheel-IRJ impact. Fig. 11(a) and (b) show the rail nodal velocities in the solution zone simulated by simulation 3 at instants 43.615 ms (output time step = 115) and 43.640 ms (output time step = 140), respectively. The color depth in the figure indicates the magnitude of the normal nodal velocity, which can be used to identify the approximate position of the wheel-rail contact patch. The darker and lighter semi-ovals indicate the leading and trailing parts of the contact patch, respectively. The tangential nodal velocities are indicated by blue arrows. The arrows point in the direction of the tangential velocity, and the arrow length is proportional to the magnitude. The stripe in the middle of each graph shows the position of the joint.

A regular wave pattern propagating from the wheel-rail contact area towards the joint can be observed in Fig. 11(a). The wave with a wavelength of approximately 6 mm is stronger around the contact patch and dissipates when propagating. When the wave front reaches the joint, a reflective wave occurs under the free boundary condition defined on the rail end at the joint. The reflective wave extends from the joint back to the contact patch and interferes with the original wave as indicated in Fig. 11(b). More obvious wave interference can be observed in the corresponding animation [33].

The wave phenomena discovered in this study are transient and normally take less than 0.1 ms from generation to disappearance. The generation process of the wave shown in Fig. 11(a) is displayed with an output time step of 1 µm in Fig. 12. The instant of the first graph (T1) is 43.603 ms, which is 0.012 ms (12 output time steps) earlier than that of Fig. 11(a). At T1, the rail surface nodal velocities appear to be distributed symmetrically with respect to the longitudinal center line. The leading and trailing parts of the contact patch can be identified by the darker and lighter semi-ovals, respectively. The region ahead of the contact area is slightly darker than that behind the contact area. The tangential velocities are mainly concentrated on the trailing part of the contact patch, and their directions are largely consistent with the wheel rolling direction. The lateral components of the tangential velocities increase with the distance to the longitudinal center line of the contact patch. At instant T2, turbulence of the nodal velocity suddenly occurs in the leading part of the contact patch. The turbulence spreads radially and consequently develops into a wave in the following instants. This turbulence is suspected to be related to the wheel-rail friction-induced instability, and studies to determine its cause are still ongoing.

Graphs of instants T3 and T6 indicate that the wave patterns are embodied in both the normal and tangential nodal velocities, and the direction of the tangential velocities are consistent with the wave propagation direction. The wave is initiated at the longitudinal position of 1244 mm (T2), and within 3 time steps, its front reaches 1254 mm (T5). Neglecting the wheel rolling distance in such a short period (less than 0.1 mm), the wave speed is estimated as 3 km/s. Both the propagation form and the speed of the produced wave are consistent with the properties of Rayleigh waves [37].

### 4.2. *Wave excited by wheel-IRJ impact*

This study also revealed that an impact wave can be generated when the wheel rolls over the joint and just touches the rail on the other side. Fig. 13 displays an impact wave produced by simulation 3 at instants 46.390 ms (output time step = 2890), 46.395 ms (output time step = 2895) and 46.400 ms (output time step = 2900). At these instants, the wheel was rolling from the left rail to the right rail, and it was in contact with both rail ends. As shown in Fig. 13, an obvious wave occurs and propagates on the rail after the joint. Compared with the wave patterns displayed in Fig. 11, the impact wave patterns displayed in Fig. 13 are mainly formed by the normal nodal velocities, and the wavelength is approximately 10 mm. The contributions of the tangential nodal velocities to the wave patterns are much less pronounced. More evident impact wave propagation can be seen in the animation [34].

In addition to the wave types displayed in Figs. 11 and 13, simulations 1 and 2 also produced waves with longer wavelengths. Fig. 14(a) and (b) show two examples produced by simulation 2 at instants 46.74 ms (output time step = 3240) and 46.762 ms (output time step = 3252), respectively. These two waves appear immediately after the whole contact patch is transferred to the rail after the joint, and their wavelengths, which are shown in Fig. 14(a) and (b), are approximately 40 mm and 20 mm, respectively. The animation [35] shows a more clear depiction of these waves. The longer-wavelength wave was not observed

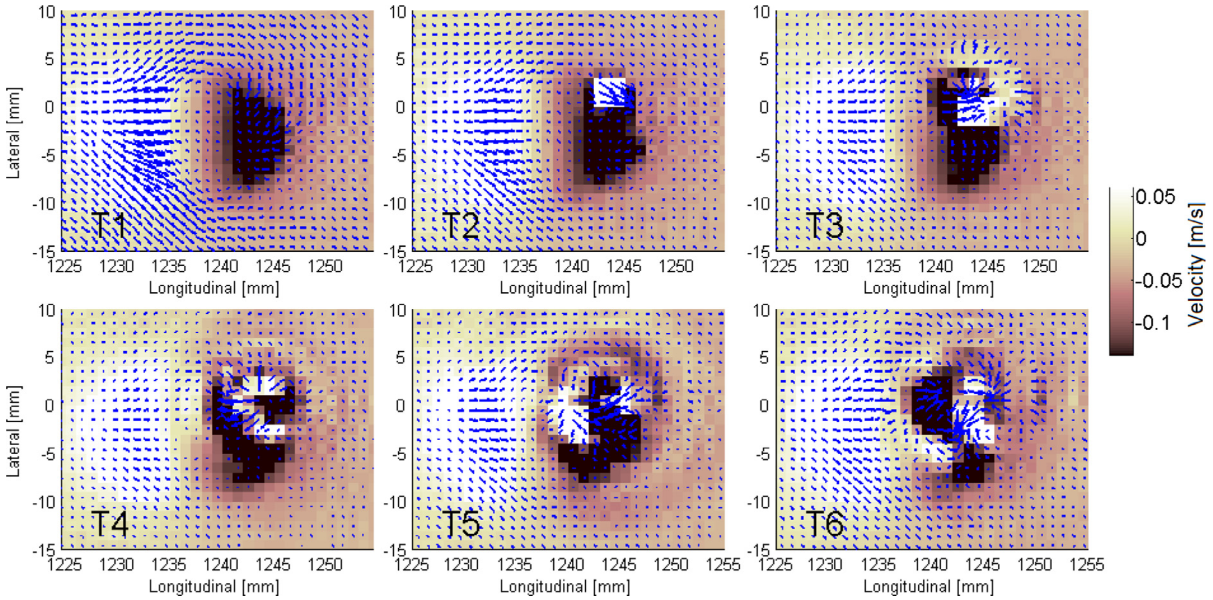

Fig. 12. Generation process of a wave.

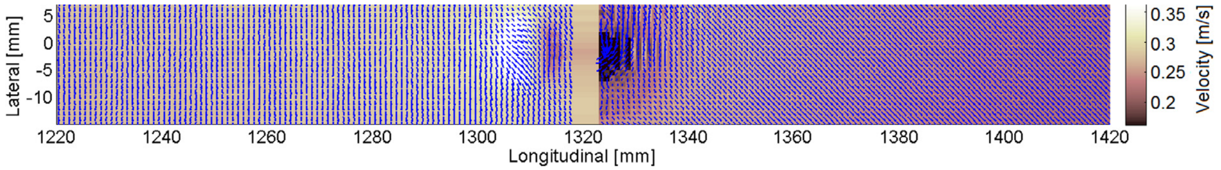

(a) Impact wave at instant 46.390 ms

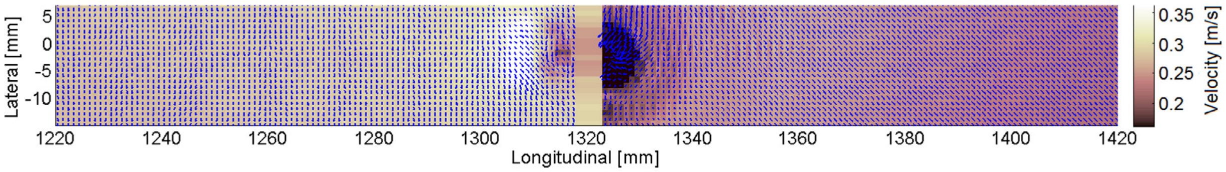

(b) Impact wave at instant 46.395 ms

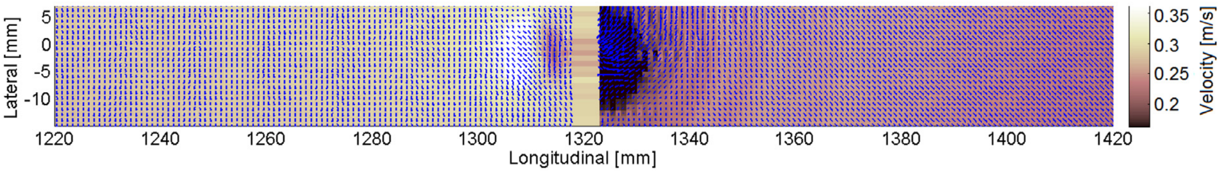

(c) Impact wave at instant 46.400 ms

Fig. 13. Impact wave pattern produced by simulation 3.

in simulation 3. The cause of these longer-wavelength waves must be further studied.

As illustrated above, wave phenomena were produced by the explicit FEM and observed in the simulated rail nodal vibration velocities in the solution zone. Because the calculations of the wheel-rail contact force and dynamics are fully coupled, the wave phenomena were also captured by the simulated wheel-rail contact force. Fig. 15 depicts the 100-kHz high-pass filtered signals of the wheel-rail contact forces in the solution zone calculated by simulations 2 and 3. Each peak of the signals shown in Fig. 15 corresponds to a wave phenomenon shown by the rail nodal velocities. Peaks 1, 2 and 3 denoted in Fig. 15 correspond to the wave phenomena shown in Figs. 11, 13 and 14, respectively. The wave phenomena corresponding to the other peaks of Fig. 15 were also produced by the simulations but are not presented here. Higher peaks correspond to more significant corresponding wave phenomena. Peak 2 shown in the lateral (upper graph) and longitudinal (bottom graph) contact force signals is less remarkable than that in the vertical force signal (middle graph), and it corresponds to the results shown in Fig. 13, which shows that the wave patterns are mainly formed by the normal nodal velocities. The cause of these high-frequency contact force peaks,

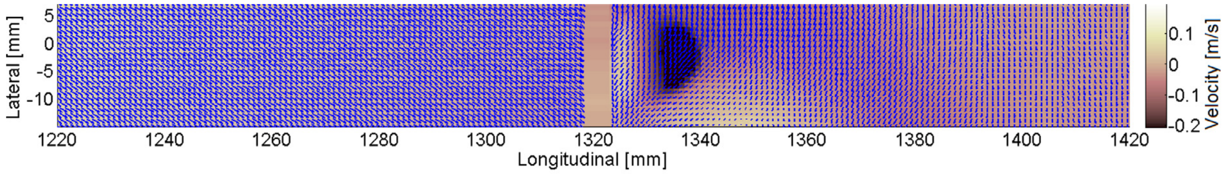

(a) Wave with a wavelength of approximately 40 mm

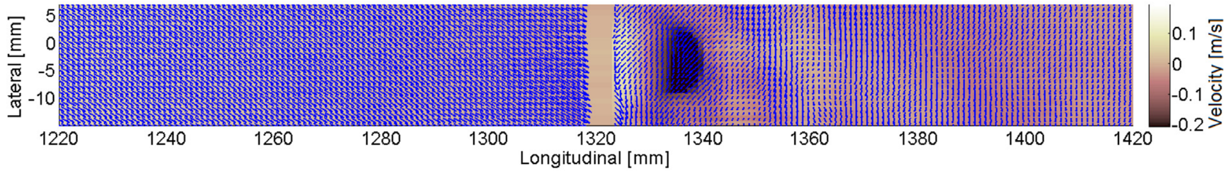

(b) Wave with a wavelength of approximately 20 mm

**Fig. 14.** Wave patterns with longer wavelengths produced by simulation 2.

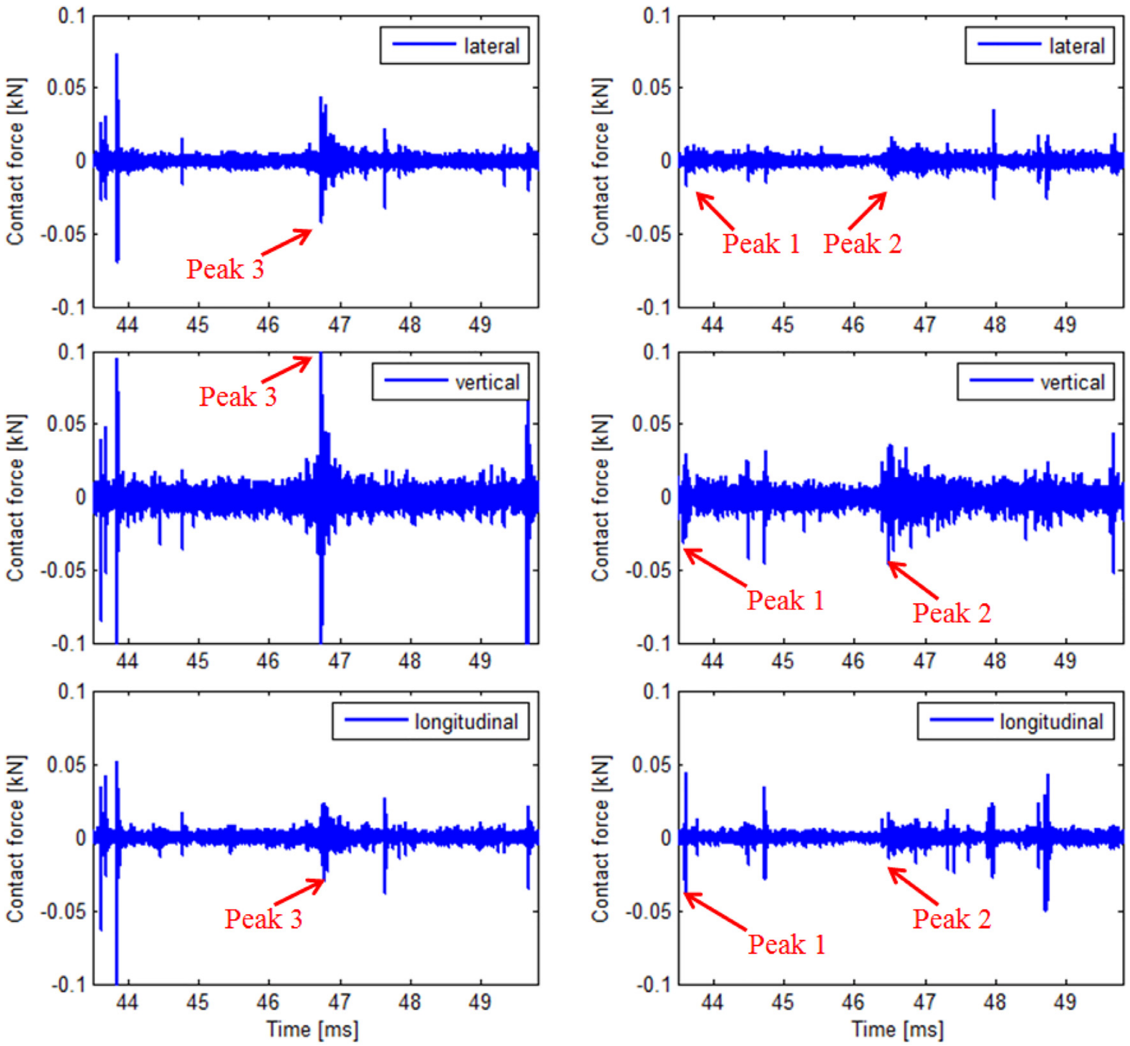

(a) Simulation 2

(b) Simulation 3

**Fig. 15.** Impact contact forces in the solution zone with a 100-kHz high-pass filter (graphs from top to bottom: lateral force, vertical force, longitudinal force).

which is likely the cause of the wave phenomena as well, has not been clearly identified in this study and will be investigated in the future.

## 5. Conclusions and future work

This paper investigated the transient contact solutions of wheel-IRJ frictional rolling impacts with dynamic effects simulated by an explicit FE wheel-IRJ dynamic interaction model, which was validated against a comprehensive field measurement in [1]. The transient solutions of impact contact with small time steps calculated in this paper include the contact patch area, stress magnitude and direction, micro-slip distribution, and rail surface nodal velocity in the vicinity of a joint. The simulated contact solutions tended to vary noticeably with the time step, indicating that dynamic effects play important roles in the wheel-IRJ impact contact. Transient positive surface shear stress, whose direction is opposite that of shear stress under ordinary tractive rolling, was discovered on the rail surface immediately after the joint. The simulated transient adhesion-slip distributions determined by the contact stresses and micro-slip solutions were verified by each other.

In addition, regular wave patterns were produced both before and during the wheel-IRJ impacts in the simulations, and these patterns reflect continuum vibrations excited by wheel-rail frictional rolling and impact contact and confirm that the simulated transient contact solutions are reliable. In combination with the conclusions drawn from [1], the presented explicit FEM is sufficient and accurate for solving wheel-IRJ impact problems by fully coupling the high-frequency dynamics of wheel and rail continua with the complex transient impact contact in one simulation.

The influence of the wheel-rail contact geometry on the transient contact solutions was also investigated in this study. The contact solutions calculated with the nominal geometry correspond well with those reported in the literature, whereas those simulated with the measured geometry show obviously non-steady-state impact effects. The good agreement between the simulated ‘footprints’ of the contact patch and the in situ running band implies that the model with the measured geometry provides more realistic predictions of the transient solutions of the impact contact at the target IRJ. Without considering the realistic contact geometries, the impact contact force and impact contact area fluctuations may be significantly underestimated.

Experimental validation of the wave phenomena produced by this study is planned to be conducted in the future by measuring high-frequency rail surface vibrations up to 1 MHz. In combination with these measurements, the source of the initiation of waves will be further investigated. Because the propagation and reflection of rail surface waves are expected to be influenced by geometric discontinuities, this study may be further developed and applied to train-borne detection of early-stage cracks on the rail head. In addition, the influence of the dynamic effects of impacts on track deterioration in the vicinity of IRJs can be studied, and the results of such studies may contribute to a sustainable IRJ design and effective maintenance in practice.

## Acknowledgments

This work was supported by the China Scholarship Council (grant No. 201206260105), the Dutch railway infrastructure manager ProRail, and the open research fund of the MOE Key Laboratory of High-speed Railway Engineering, Southwest Jiaotong University.

## Supplementary materials

Supplementary material associated with this article can be found, in the online version, at doi:10.1016/j.ijmecsci.2018.02.025.

## References

[1] Yang Z, Boogaard A, Chen R, Dollevoet R, Li Z. Numerical and experimental study of wheel-rail impact vibration and noise generated at an insulated rail joint. Int J Impact Eng 2018;113:29–39.
[2] Chen YC, Kuang JH. Contact stress variations near the insulated rail joints. Proc Inst Mech Eng Part F 2002;216:265–73.
[3] Hertz H. Ueber die Berührung fester elastischer Körper. Journal für die reine und angewandte Mathematik (Crelle’s Journal) 1882:1882.
[4] Chen YC, Chen LW. Effects of insulated rail joint on the wheel/rail contact stresses under the condition of partial slip. Wear 2006;260:1267–73.
[5] Carter FW. On the action of a locomotive driving wheel. Proc R Soc Lond A-Conta 1926;112:151–7.
[6] Wen ZF, Jin XS, Zhang WH. Contact-impact stress analysis of rail joint region using the dynamic finite element method. Wear 2005;258:1301–9.
[7] Cai W, Wen ZF, Jin XS, Zhai WM. Dynamic stress analysis of rail joint with height difference defect using finite element method. Eng Fail Anal 2007;14:1488–99.
[8] Sandstrom J, Ekberg A. Numerical study of the mechanical deterioration of insulated rail joints. Proc Inst Mech Eng F-J Rai 2009;223:265–73.
[9] Mandal NK, Dhanasekar M. Sub-modelling for the ratchetting failure of insulated rail joints. Int J Mech Sci 2013;75:110–22.
[10] Mandal NK. Finite element analysis of the mechanical behaviour of insulated rail joints due to impact loadings. Proc Inst Mech Eng F-J Rai 2016;230:759–73.
[11] Zong N, Wexler D, Dhanasekar M. Structural and material characterisation of insulated rail joints. Electron J Struct Eng 2013;13:75–87.
[12] Zong N, Dhanasekar M. Minimization of railhead edge stresses through shape optimization. Eng Optim 2013;45:1043–60.
[13] Zong N, Dhanasekar M. Hybrid genetic algorithm for elimination of severe stress concentration in railhead ends. J Comput Civil Eng 2015;29:04014075.
[14] Zong N, Dhanasekar M. Sleeper embedded insulated rail joints for minimising the number of modes of failure. Eng Fail Anal 2017;76:27–43.
[15] Li ZL, Zhao X, Dollevoet R, Molodova M. Differential wear and plastic deformation as causes of squat at track local stiffness change combined with other track short defects. Vehicle Syst Dyn 2008;46:237–46.
[16] Pletz M, Daves W, Ossberger H. A wheel set/crossing model regarding impact, sliding and deformation-Explicit finite element approach. Wear 2012;294:446–56.
[17] Ayasse JB, Chollet H. Determination of the wheel rail contact patch in semi-Hertzian conditions. Vehicle Syst Dyn 2006;43:161–72.
[18] Kalker JJ. Three-dimensional elastic bodies in rolling contact. 1st ed. Netherlands: Springer; 1990.
[19] Piotrowski J, Kik W. A simplified model of wheel/rail contact mechanics for non-Hertzian problems and its application in rail vehicle dynamic simulations. Vehicle Syst Dyn 2008;46:27–48.
[20] Zhao X, Zhao X, Liu C, Wen Z, Jin X. A study on dynamic stress intensity factors of rail cracks at high speeds by a 3D explicit finite element model of rolling contact. Wear 2016.
[21] Wei ZL, Li ZL, Qian ZW, Chen R, Dollevoet R. 3D FE modelling and validation of frictional contact with partial slip in compression-shift-rolling evolution. Int J Rail Transp 2016;4:20–36.
[22] Yang Z, Li ZL, Dollevoet R. Modelling of non-steady-state transition from single-point to two-point rolling contact. Tribol Int 2016;101:152–63.
[23] Zhao X, Li ZL. The solution of frictional wheel-rail rolling contact with a 3D transient finite element model: Validation and error analysis. Wear 2011;271:444–52.
[24] Deng X, Qian Z, Dollevoet R. Lagrangian explicit finite element modeling for spin-rolling contact. J Tribol 2015;137:041401.
[25] Mulvihill DM, Kartal ME, Nowell D, Hills DA. An elastic–plastic asperity interaction model for sliding friction. Tribol Int 2011;44:1679–94.
[26] Wriggers P. Computational contact mechanics. Berlin Heidelberg: Springer; 2006.
[27] Flanagan DP, Belytschko T. A uniform strain hexahedron and quadrilateral with orthogonal hourglass control. Int J Numer Methods Eng 1981;17:679–706.
[28] Zong N, Dhanasekar M. Experimental studies on the performance of rail joints with modified wheel/railhead contact. Proc Inst Mech Eng F-J Rai 2014;228:857–77.
[29] Hallquist JO, Goudreau GL, Benson DJ. Sliding interfaces with contact-impact in large-scale Lagrangian computations. Comput Methods Appl Mech Eng 1985;51:107–37.
[30] Eadie DT, Santoro M, Powell W. Local control of noise and vibration with KELTRACK™ friction modifier and Protector® trackside application: an integrated solution. J Sound Vib 2003;267:761–72.
[31] Zhao X, Li ZL. A three-dimensional finite element solution of frictional wheel-rail rolling contact in elasto-plasticity. Proc Inst Mech Eng J-J Eng 2015;229:86–100.
[32] Hallquist JO. LS-DYNA theory manual; 2006.
[33] Animation for Fig. 11, https://youtu.be/tWyWKw9XxRI; [accessed 16.11.22] in.
[34] Animation for Fig. 13, https://youtu.be/fAg99j6kquI; [accessed 16.11.22] in.
[35] Animation for Fig. 14, https://youtu.be/eHh24SnWDFQ; [accessed 16.11.22] in.
[36] Zhao X, Li Z. A solution of transient rolling contact with velocity dependent friction by the explicit finite element method. Eng Comput 2016;33:1033–50.
[37] Telford WM, Geldart LP, Sheriff RE. Applied geophysics. Cambridge University Press; 1990.